JACS
JOURNAL OF THE AMERICAN CHEMICAL SOCIETY
pubs.acs.org/JACS
Perspective

Insights into the Structure and Dynamics of Metal–Organic Frameworks via Transmission Electron Microscopy

Xinyi Gong, Karthikeyan Gnanasekaran, Zhijie Chen, Lee Robison, Megan C. Wasson, Kyle C. Bentz, Seth M. Cohen,* Omar K. Farha,* and Nathan C. Gianneschi*

Cite This: J. Am. Chem. Soc. 2020, 142, 17224–17235
Read Online
ACCESS | Metrics & More | Article Recommendations

ABSTRACT: Metal–organic frameworks (MOFs) are hybrid materials composed of metal ions and organic linkers featuring high porosity, crystallinity, and chemical tunability at multiple length scales. A recent advancement in transmission electron microscopy (TEM) and its direct application to MOF structure–property relationships have changed how we consider rational MOF design and development. Herein, we provide a perspective on TEM studies of MOFs and highlight the utilization of state-of-the-art TEM technologies to explore dynamic MOF processes and host–guest interactions. Additionally, we provide thoughts on what the future holds for TEM in the study of MOFs.

1. INTRODUCTION

Metal–organic frameworks (MOFs) are hybrid materials comprised of metal ions or clusters and multitopic organic linkers.[1−4] These distinct components self-assemble to form highly porous, crystalline, and tunable frameworks that have shown potential for a variety of applications, including gas storage,[5−9] separation,[10−12] catalysis,[13−16] water capture,[17−20] and drug delivery.[21−23] Postsynthetic metal-cation exchange and ligand functionalization allow for further modification of MOF microstructures at multiple length scales, expanding their scope and functionality.[24,25] A deep mechanistic understanding of MOF formation, phase transition, guest molecule interactions, and other dynamic processes are important to further develop the rational design and exploitation of MOFs.

MOF and MOF-like materials are commonly characterized by scanning electron microscopy (SEM), powder X-ray diffraction (PXRD), single-crystal X-ray diffraction (SXRD), gas sorption (e.g., surface area, pore size), thermal gravimetric analysis (TGA), and transmission electron microscopy (TEM). In comparison to many of the more conventional characterization techniques that can only be applied to bulk samples, TEM is unique in that it permits direct structural and dynamic information on individual MOF crystallites. However, TEM of MOF materials remains challenging due to the sensitivity of MOFs to high energy electrons, which limits electron dose conditions, accessible image resolution, and signal-to-noise ratio for reasonable structural and dynamic characterization.

In the transmission electron microscope, the accelerated high energy electrons emitted from an electron source interact with a thin MOF specimen (Figure 1). The basic beam path of the two main TEM modes, bright-field (BF) TEM and annular dark-field (ADF) scanning TEM (STEM), are shown in Figure 1a. In both modes, some electrons are deflected by the electrostatic field of the atomic nuclei, valence electrons of the specimen atoms, or nearly collide with the atomic nuclei of the specimen atoms resulting high-angle deflections and backscattering (Figure 1b). A direct interaction between the incident electrons and the nucleus of the specimen atom introduces knock-on atomic displacement. Knock-on displacement depends on the sample-specific threshold energy; hence, reducing the TEM accelerating voltage below some threshold value will largely eliminate the damage.[26−28] Energy transfer from the inelastic scattering events can ionize the specimen atoms leading to radiolytic processes such as chemical bond cleavage, formation of free radicals, X-ray emission, and phonon scattering. Radiolysis is often a temperature dependent mechanism. Hence, cooling the sample holder with liquid nitrogen can reduce the damage by typically a factor of 3–10.[29,30] In addition, damage to the structure is also introduced by the heating and electrostatic charging of the insulating materials. Reduction of beam current mitigates damage caused by heating and charging.[31] All these radiation effects are heavily electron dose dependent, and multiple mechanisms contribute to the structural damage.

To reduce radiation damage, special "low dose" methods commonly used in cryogenic TEM (cryo-TEM) can be applied to MOF materials.[32,33] There is no single critical value for the dose threshold (D_c) for MOFs. It varies over a range depending on the MOF structure, type of imaging, and dose rate. Notably, the presence of guest molecules, such as water or pyridine coordinated to the inorganic nodes of MOFs, can further affect MOF beam sensitivities.[34] Figure 1c summarizes several examples of MOFs stable enough to be studied by

Received: August 14, 2020
Published: September 18, 2020

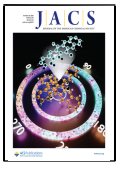

https://dx.doi.org/10.1021/jacs.0c08773
J. Am. Chem. Soc. 2020, 142, 17224–17235

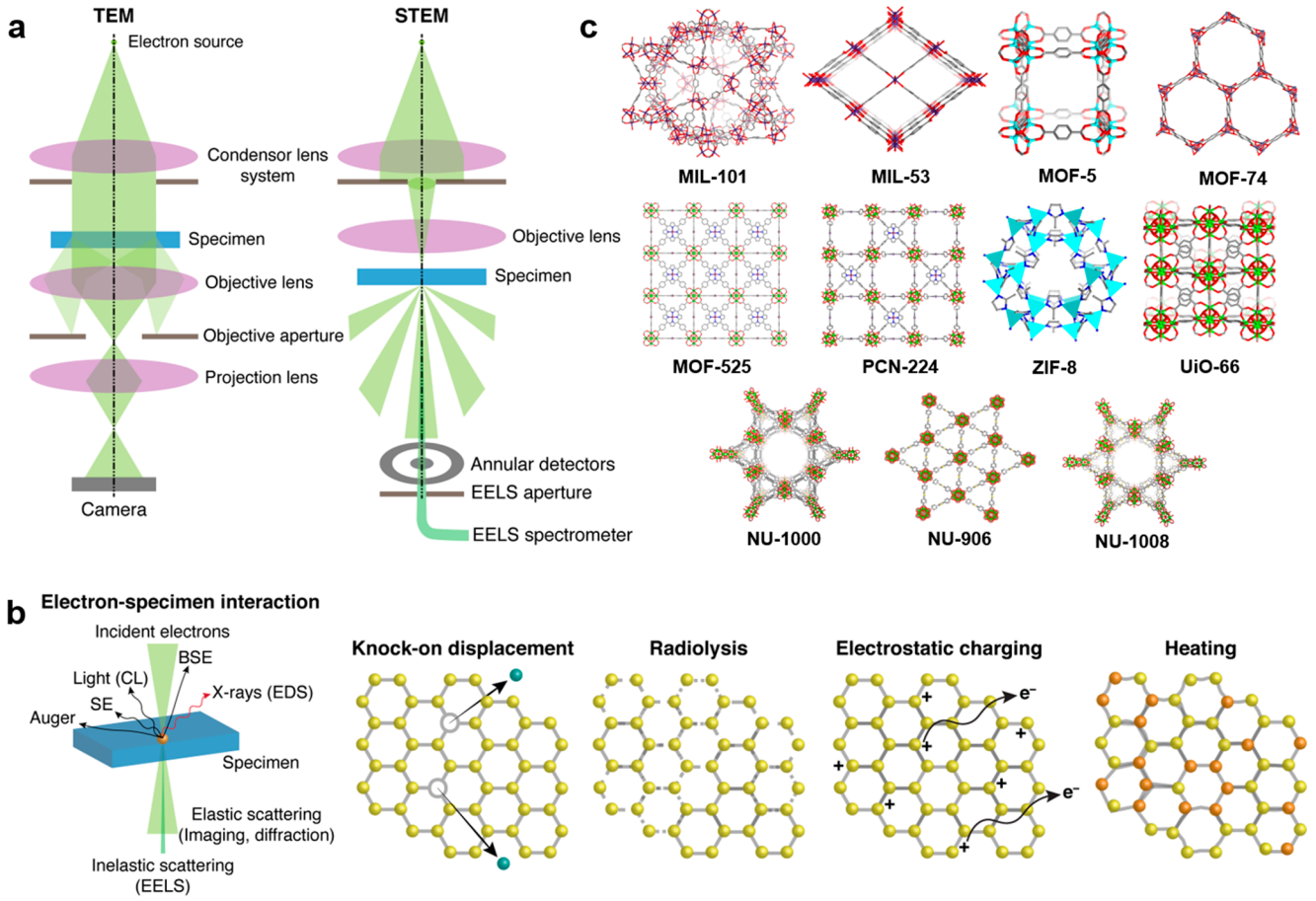

Figure 1. (a) Schematic illustration of electron beam path in TEM and STEM modes. (b) Electron-specimen interaction and beam damages. EELS, EDS, CL, SE, and BSE refer to electron energy loss spectroscopy, energy dispersive X-ray spectroscopy, cathodoluminescence, secondary electron, and back scattering electron, respectively. (c) MOF crystal structures discussed in this perspective. Atom color scheme: Zr, green; Cr, purple; Zn, turquoise; Mg, blue gray; C, gray; O, red; N, blue; Br, yellow, Pt, plum. H atoms are omitted for clarity.

Table 1. Examples of Electron Doses in TEM of MOFs

MOF	Electron Dose ($e^{-}Å^{-2}$)	MOF	Electron Dose ($e^{-}Å^{-2}$)
MIL-101	~8[35]	MIL-53	~5[36]
MOF-5	0.6[29]	MOF-74	~2.5[37]
ZIF-8	4.1[38]	UiO-66	~12[39]
MOF-525 PCN-224	~5[40]	NU-906 NU-1008	~5[41]

TEM at reasonable electron fluence, and each is discussed in this Perspective. The electron doses used in the acquisition of TEM data for these MOFs are commonly very low (Table 1).

Recent developments in camera and detector technology, such as direct-detection electron-counting (DDEC) cameras with extremely high detective quantum efficiency (DQE), permit the capture of electron density maps with extremely low doses,[42,43] which has made the use of TEM more suitable for the study of MOFs. Automated tools mitigating manual intervention also enable recording high quality data with minimal electron doses.[44,45] During the past several years, the utilization of DDEC cameras has enabled several breakthrough developments in high resolution TEM (HRTEM) of MOFs, revealing the structures of MOFs at a scale and resolution not observable by other characterization techniques.[38,39,46] Similarly, low dose imaging facilitates in situ TEM elucidation of dynamic processes of MOFs, providing mechanistic understanding of these materials. In situ hot stage TEM,[47] liquid cell TEM (LCTEM),[41,48−50] and environmental TEM (ETEM)[36] offer routes to directly observe MOF dynamics under a vacuum, in liquids, and in gas phase, respectively. These tools utilize hot stage or liquid cell holders that can be inserted into a microscope, or manifold systems to introduce gas, to create different environments around the specimen. These in situ investigations remain in a nascent stage in the MOF field and offer great potential in further exploring mechanisms of a wide range of phenomena.

In this Perspective, we discuss some of the groundbreaking discoveries of the structure and dynamics of MOFs that utilized advanced TEM techniques in recent years. We illustrate how TEM techniques have changed the conventional wisdom concerning MOF characterization, with the methods emerging as indispensable to the field.

2. DISCUSSION

2.1. Structural Analysis of MOFs. *2.1.1. Nanocrystal Structures.* One of the prevalent uses of TEM to study MOFs is to provide direct proof of the crystalline structure. Conventionally, SXRD is used to determine the structure of crystalline materials that produce sufficiently large crystals to be studied, generally between 10 and 250 μm in size. However,

https://dx.doi.org/10.1021/jacs.0c08773
J. Am. Chem. Soc. 2020, 142, 17224−17235

the growing of large single crystals of MOFs often poses significant challenges. 3-Dimensional electron diffraction (3D-ED) techniques enabled ab initio structure determination of nanosized MOF crystals, a size domain too small to be solved by SXRD. With 3D-ED, the 3D reciprocal space reconstruction can resolve unit cell parameters and space groups.[51−56] For example, continuous rotation electron diffraction (cRED) determined and refined the isoreticular MOF structures, PCN-415 ($[Ti_8Zr_2O_{12}(CH_3COO)_{16}(bdc)_6]$, bdc^{2-} = 1,4-benzene dicarboxylate; **fcu** net) and PCN-416 ($[Ti_8Zr_2O_{12}(CH_3COO)_{16}(ndc)_6]$, ndc^{2-} = 2,6-naphthalene dicarboxylate; **fcu** net), which showed excellent agreement with Rietveld refinement against PXRD data (Figure 2).[55] Notably, the atomic structure obtained by cRED has been shown as reliable and accurate as that obtained by SXRD.[57]

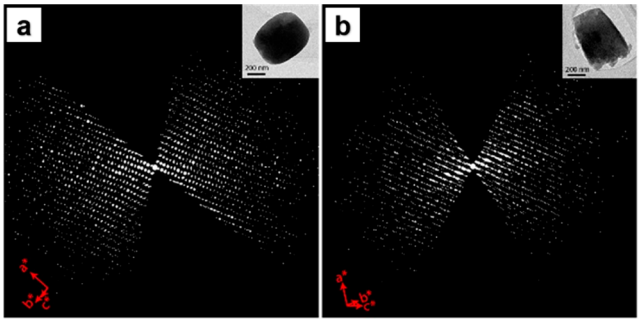

Figure 2. Reconstructed 3D reciprocal lattice of (a) PCN-415 and (b) PCN-416 with insets showing the corresponding crystals. Reproduced with permission from ref 55 (https://pubs.acs.org/doi/10.1021/acscentsci.7b00497). Copyright 2017 American Chemical Society.

In addition to 3D-ED studies, the direct visualization of MOF structures with HRTEM under low dose conditions is an emerging field that provides direct imaging of the MOF structure. One early notable HRTEM study on MIL-101 ($[Cr_3(O)F(bdc)_3(H_2O)_2]$; **mtn** net) provided the nanocrystal structures from different projected orientations.[58] HRTEM imaged pore configurations of MIL-101 and directly observed pristine hexagonal packing of tunnels for the first time. In a separate study, to image the pore structures of an intact MOF-5 ($[Zn_4O(bdc)_3]$; **pcu** net) particle, HRTEM was conducted with cooling of the sample using liquid nitrogen and at low accelerating voltage (80 kV) to reduce beam induced damage.[29]

HRTEM studies also examined the structures of members of an isoreticular series of MOF-74 ($[M_2(DOT)]$, M = Zn or Mg, DOT = 2,5-dioxidoterephthalate; **msf** net) from the original DOT link of one phenylene ring to two (II), three (III), four (IV), five (V), six (VI), seven (VII), nine (IX), and eleven (XI) (Figure 3a) that display systematically expanded pore apertures.[37] The arrangement and the size of pores were observed along the *c* axis for MOF-74-VII and IX, and the lattice spacings derived from fast Fourier transform (FFT) of HRTEM images matched well with those from PXRD, confirming the nanostructures of the isoreticular series of MOF-74 (Figure 3b,c). Subsequently, high-voltage (300 kV) C_s-corrected STEM techniques provided near-atomic resolution information on MOF-74 (Zn).[59,60] Zn(II) clusters could be identified in both high-angle annular dark field (HAADF) and annular bright field (ABF) images, and in ABF, signals of

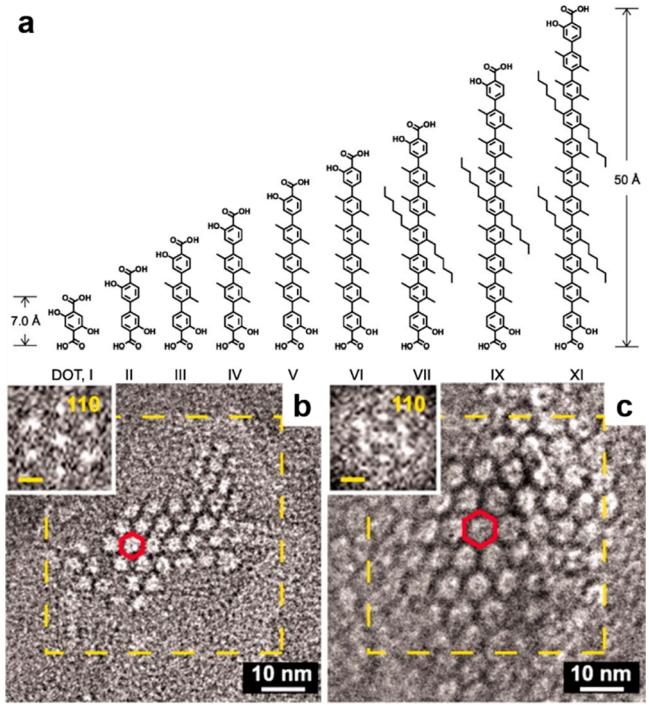

Figure 3. (a) Structures of DOT linkers. HRTEM of (b) IRMOF-74-VII and (c) IRMOF-74-IX, with insets of FFT patterns of the dashed square area in the original images. Reproduced with permission from ref 37. Copyright 2012 American Association for the Advancement of Science.

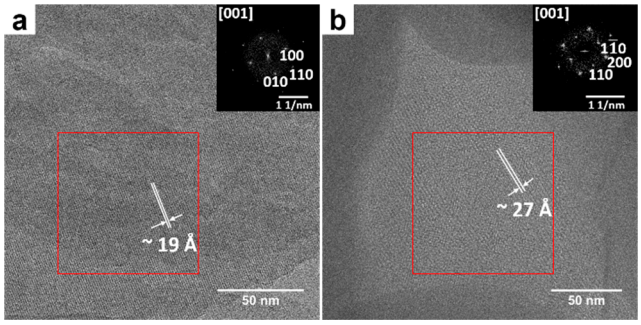

Figure 4. HRTEM of (a) MOF-525(Pt) and (b) PCN-224(Pt), with insets of FFT patterns of the red square areas, cropped at the predominant lattice fringes. Reproduced with permission from ref 40. Copyright 2019 American Chemical Society.

Zn(II) atomic columns for some certain clusters were observed.

While HRTEM can readily discern pore size and image metal nodes, the electron dense metal nodes often dominate the contrast in TEM such that structural organic linkers remain invisible. For some MOF polymorphs, linker orientation is a defining feature, which necessitates imaging of the organic ligand as well. For example, MOF-525 ($[Zr_6O_4(OH)_4(TCPP\text{-}H_2)_3]$, TCPP-$H_2$ = tetrakis(4-carboxyphenyl)porphyrin; **ftw** net), and PCN-224 ($[Zr_6O_4(OH)_4(TCPP\text{-}H_2)_{1.5}(H_2O)_6(OH)_6]$; **she** net) are a pair of MOFs with exactly the same arrangement of Zr_6 nodes, yet they differ in the arrangement of their porphyrinic linkers.[40] Despite their alternate phase, they display similar sorption behavior and PXRD patterns, precluding the ability for traditional MOF characterization techniques to distinguish between them. While the two MOFs

https://dx.doi.org/10.1021/jacs.0c08773
J. Am. Chem. Soc. 2020, 142, 17224−17235

with free base linkers (TCPP-H_2) appeared structurally equivalent via regular HRTEM, modification of their porphyrinic linkers with Pt (TCPP-Pt) to generate enough image contrast enabled unambiguous identification of the two structures via the difference in the lattice spacings (Figure 4).

An interesting subset of recently developed MOF-based materials are MOFs where the organic component is a polymer ligand, rather than a molecular organic ligand (Figure 5a).[61,62] These so-called polyMOFs offer the potential to combine the material properties of MOFs and polymers. Moreover, as compared to their molecular-derived counterpart MOFs, polyMOFs displayed highly unusual bulk crystal morphologies (Figure 5b).[63] While several studies examined the effect of polymer architecture and framework identity on the resulting crystal morphology, only recently has the interior structure of these materials been investigated. Following ultramicrotome slicing on polyMOFs, TEM imaging observed alternating layers of metal-rich and metal-deficient domains within the interior structure of UiO-66-based polyMOFs constructed from block polymers (Figure 5c). Further analysis by EDS mapping confirmed the layers alternate between high and low concentrations of Zr(IV), indicating distinct layers of MOF and amorphous, metal-free layers.

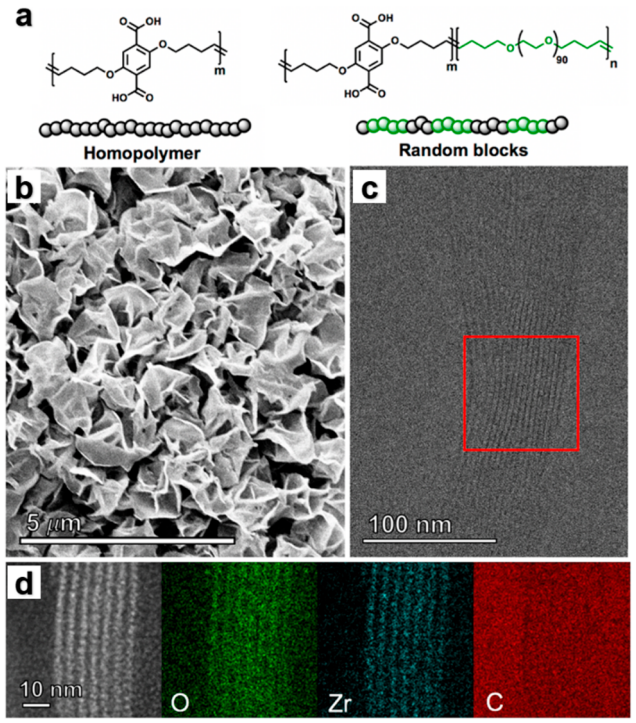

Figure 5. HAADF-STEM analysis of polyUiO-66 derived from a random block polymer with PEG. (a) Structure of polymer ligands used for polyMOFs, showing both homopolymer (left) and a random block polymer with PEG (right). (b) SEM image of UiO-66 from PEG-containing block polymer ligand. (c) TEM image of ultramicrotomed slice of polyMOF from part b. (d) EDS mapping of subsection outlined in part c showing alternating Zr-rich and Zr-deficient layers. Reproduced with permission from ref 63. Copyright 2020 Royal Society of Chemistry.

2.1.2. Surface and Interfacial Structures. The surface structures of MOF particles offer insights into the mechanism of molecular assembly, which often affects particle shapes and sizes.[64,65] Imparting control over the surface and interfacial structures of MOFs can subsequently alter mass transport properties for targeted guest molecules.[66,67] With the advent of the DDEC camera, HRTEM on MOFs achieved atomic level resolution, allowing for the investigation of these local structures of MOFs. TEM images acquired with a DDEC camera identified individual Zn(II) atomic columns and organic linkers in ZIF-8 ([Zn(2-methylimidazole)$_2$]; **sod** net) with a resolution of 2.1 Å (Figure 6a).[38] The surface of ZIF-8 particles terminated in the armchair motif (Figure 6b). Furthermore, the 110 surfaces of two attached particles exhibited an arm-to-notch configuration through an additional interfacial layer of ligands. However, these zone-axis images of ZIF-8 were obtained by the inefficient sampling of randomly oriented particles.

To overcome the time-intensive sampling of particles to image a zone axis, a program was developed to automatically align the zone axis for crystals with initial orientations that were close to a zone axis within 5°.[39] The study of UiO-66(Zr) ([$Zr_6O_4(OH)_4(bdc)_6$]; **fcu** net) resolved the Zr(IV) atomic columns within the Zr_6 nodes and benzene rings with face-on configurations (Figure 6c). Moreover, the imaging revealed the presence of both ligand-free and ligand-capped surfaces (Figure 6d) in which the major exposed 111 surface terminated with linkers (Figure 6e), while the kink positions between 100 and 111 facets exposed Zr(IV) clusters (Figure 6f).

With the same methods, the surface structures of MIL-101 were examined.[35] Even though the low contrast and structural complexity of the MOF prevented identification of the linkers,

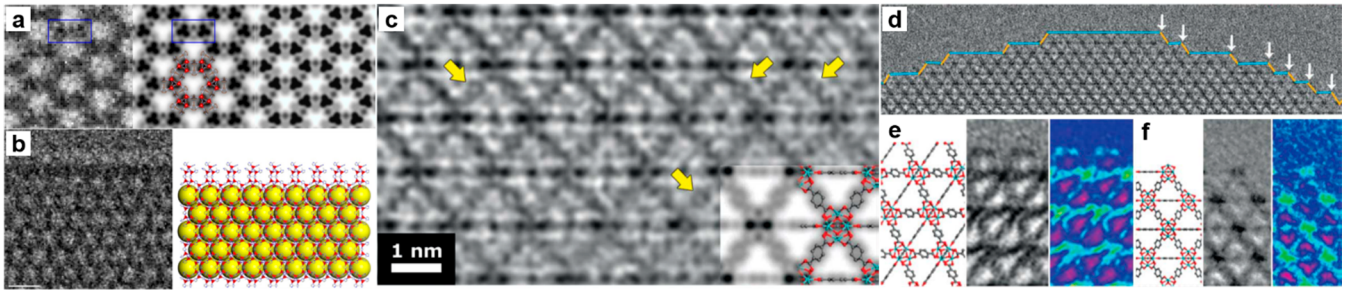

Figure 6. HRTEM of ZIF-8: (a) left, contrast transfer function (CTF)-corrected and denoised image; middle, symmetry-imposed and lattice-averaged image; right, simulated projected potential map. (b) HRTEM image and structural model of the ZIF-8 (110) surface. Reproduced with permission from ref 38. Copyright 2017 Springer Nature. HRTEM of UiO-66(Zr): (c) CTF-corrected denoised image. (d) A truncation surface, showing crystal growth steps involving small 100 facets and 111 facets. (e) Ligand-terminated 111 surface. (f) Metal-terminated 100/111 kink. Reproduced with permission from ref 39. Copyright 2018 American Association for the Advancement of Science.

https://dx.doi.org/10.1021/jacs.0c08773
J. Am. Chem. Soc. 2020, 142, 17224−17235

the arrangements of Cr(III) clusters revealed different degrees of opening in the surface mesoporous cages when the samples were synthesized with different additives. Moreover, vacuum heating treatment of the samples at specific temperatures altered these the opening degrees as observed via HRTEM.

2.1.3. Defects. Defects in MOFs directly affect their pore structures and open metal sites. Judicious control over defects provides novel opportunities in sorption, catalysis, as well as magnetic and electrical properties.[68] An understanding of the density, distribution, and types of defects is essential to control crystal quality and to manipulate targeted functionalities. Attempts on utilizing HRTEM to image MOF defects first started with the characterization of defective UiO-66(Hf) ($[Hf_6O_4(OH)_4(bdc)_6]$; **fcu** net).[69] ED generated both parent and superlattice reflections, and TEM imaging of the crystallite indicated a complex microstructure with domain boundaries resulting from mass contrast. However, beam sensitivity of the sample prevented further investigation through HRTEM.

Recently, the direct imaging of defects in UiO-66(Zr) was achieved at subunit-cell resolution, and HRTEM showed the coexistence of both missing-linker and missing-node defects.[46] When defective structures were compared with perfect structures, the absence of contrast for organic linkers was indicative of missing-linker defects (Figure 7a,b). Defective

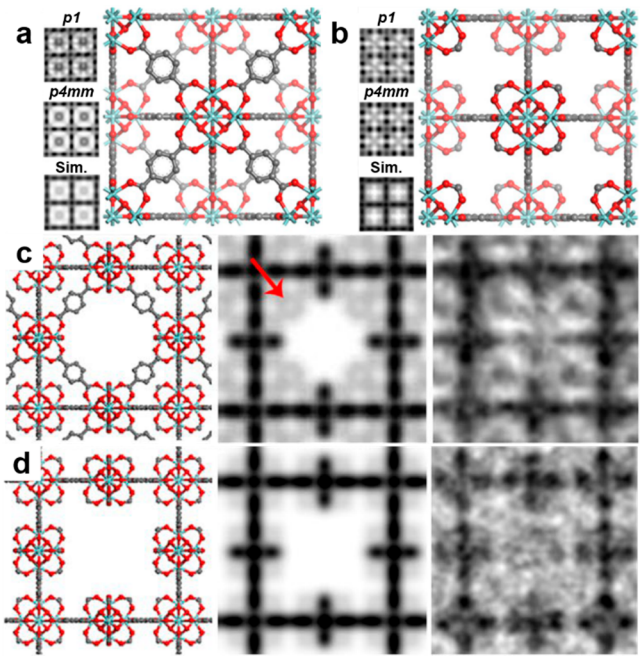

Figure 7. HRTEM analysis of missing-linker defects: *p*1-averaged image (top), symmetry-imposed image (middle), simulated projected potential (bottom), and projected structural model of (a) perfect region and (b) missing-linker region along the [001] zone axis. HRTEM analysis of missing-node defects: projected structural model (left), simulated projected potential map (middle), and experimental image (right) of (c) **reo** structure and (d) **scu** structure. Reproduced with permission from ref 46. Copyright 2019 Springer Nature.

UiO-66(Zr) crystals predominantly contained missing-linker domains with the 3-periodic **bcu** topology, while perfect regions without defects were rare. Throughout the sample, it was always observed that only a few unit cells possessed missing node-domains correlating with the superlattice reflections. HRTEM identified two types of missing-node defects classified by the presence or absence of the face-on linkers, which surrounded, but did not connect to, the missing node. These defects respectively correspond to **reo** and **scu** nets (Figure 7c,d).

2.1.4. Host–guest Interactions. Host–guest interactions govern the chemistry of storage, separation, and catalysis applications of MOF materials. Gaining insights into the interactions between host MOFs and guest molecules enhances the loading process for guest molecules inside MOFs and enables the study of interactions between the frameworks and the guests. One technique for studying such interactions includes electron tomography (ET).[70] This approach provides three-dimensional information needed to confirm the embedding of metal nanoparticles,[71−74] drugs,[75] enzymes,[76] and other guest molecules inside MOFs. Beyond merely probing guest encapsulation, the technique elucidates the filling degree and distribution of guests relative to the bulk of MOFs. For example, ET showed 3D homogeneously distributed mesopores filled by doxorubicin molecules in ZIF-8 particles (Figure 8).[75] Altering the concentration of guest molecules tuned the size of these mesopores, as detected by ET.

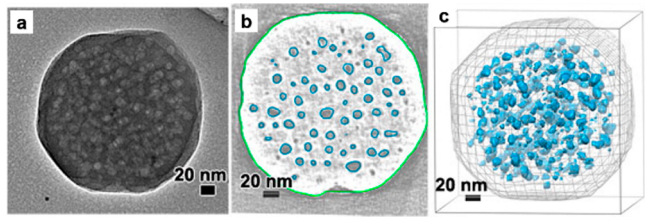

Figure 8. Distribution of mesopores in a doxorubicin@ZIF-8 particle by ET. (a) TEM image. (b) Cross-section of the RT with the mesopores indicated by blue lines. (c) 3D distribution of the mesopores. Reproduced with permission from ref 75. Copyright 2015 American Chemical Society.

Additionally, investigating guest location and distribution in the individual MOF pores can extract more detailed information about host–guest interactions and related properties of these materials. For example, ADF-STEM directly imaged Pt nanoclusters deposited via atomic layer deposition (ALD) inside MIL-101.[73] This technique demonstrated confined growth of Pt nanoparticles inside the pores of MIL-101 as determined by the resulting nanoparticle size tailored to the pore size of MIL-101. The nanoparticles were observed at the positions of both small and large pores of MIL-101 in 2D projection (Figure 9). Moreover, ET confirmed the Pt species were inside the bulk of MIL-101. The combination of ADF-STEM and ET indicated the presence of Pt nanoparticles in both large and small pores of MIL-101.

Beyond the extraction of guest position information, direct imaging of encapsulated species within MOF pores has been achieved using HRTEM. For example, HRTEM directly imaged encapsulated $Mn_{12}Ac$ single-molecule magnets (SMMs) within the pores of NU-1000 ($[Zr_6O_4(OH)_4(TBAPy)_2(OH)_4(H_2O)_4]$, TBAPy = 1,3,6,8-tetrakis(p-benzoate)pyrene; **csq** net).[77] Ultramicrotome sliced $Mn_{12}Ac$@NU-1000 particle thin sections facilitated imaging along the [001] zone axis of NU-1000, which also proved the actual embedding of $Mn_{12}Ac$ inside instead of on the surface of MOF particles. The image contrast in HRTEM clearly identified individual particles with a diameter of around 2

https://dx.doi.org/10.1021/jacs.0c08773
J. Am. Chem. Soc. 2020, 142, 17224−17235

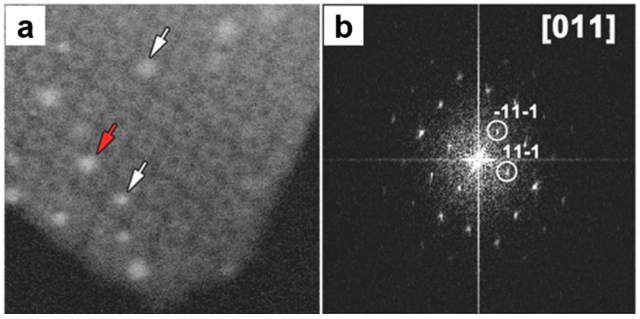

Figure 9. (a) ADF-STEM image and (b) FFT of MIL-101 crystal with Pt nanoparticles. From projection, white arrows point to nanoparticles at small cage positions, the red arrow points to nanoparticles at large cage positions. Reproduced with permission from ref 73. Copyright 2016 Wiley.

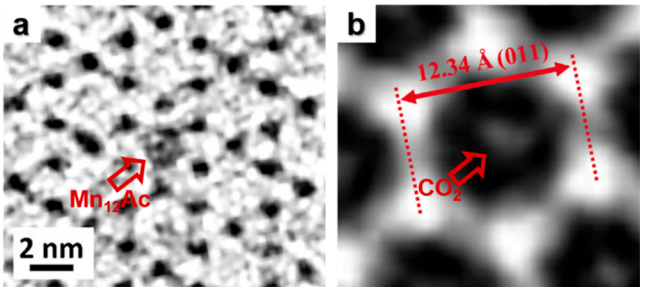

Figure 10. (a) HRTEM image of $Mn_{12}Ac$@NU-1000 along the [001] zone axis of NU-1000. Reproduced with permission from ref 77. Copyright 2019 American Chemical Society. (b) Cryo-TEM image of CO_2@ZIF-8 along [111] axis of ZIF-8. Reproduced with permission from ref 78. Copyright 2019 Elsevier.

nm located in the hexagonal channels of NU-1000 (Figure 10a).

Promising MOF-based applications include the storage and separation of small guest molecules, namely gases, which presents significant challenges for direct imaging. Recently, cryo-TEM was utilized to stabilize adsorbed CO_2 in ZIF-8, which achieved the direct imaging of subnanometer guest molecules inside MOF pores.[78] The cryogenic conditions helped to preserve the ZIF-8 structure and inhibit CO_2 desorption from ZIF-8 for HRTEM. Bright contrast was observed in the center of hexagonal window in CO_2 filled ZIF-8 (Figure 10b) whereas the density was absent for the empty ZIF-8. Moreover, a 3% lattice expansion occurred upon CO_2 adsorption, implying a strong interaction between CO_2 and ZIF-8. Investigation along other zone axes revealed the existence of more than one binding site.

2.2. Dynamic Analysis of MOFs. *2.2.1. MOF Formation.* An understanding of MOF formation in solution is important in developing new synthetic MOF chemistry as well as optimizing MOF structures for targeted performance. LCTEM provides spatiotemporal resolution to study this phenomenon, allowing for the direct observation of particle nucleation, growth, and self-assembly. The first application of in situ LCTEM on MOFs observed the real-time growth processes of ZIF-8 (Figure 11).[48] Indeed, this was one of the first such studies investigating self-assembled materials more generally. Here, beam damage studies showed damage and dissolution of MOF particles at 200 kV above a cumulative electron dose (or total fluence) of 400 $e^{-}Å^{-2}$ with the electron dose rate (or electron flux) of 3.25 $e^{-}Å^{-2}s^{-1}$. However, when the electron

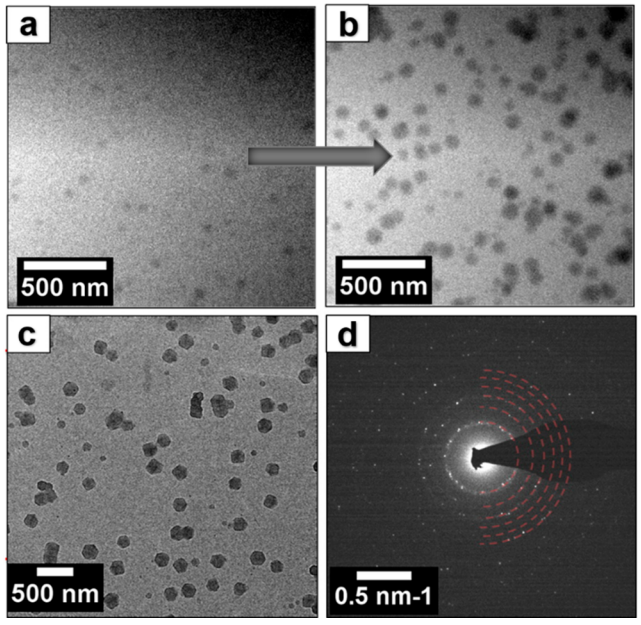

Figure 11. (a, b) Snapshots from the LCTEM movie showing growth of ZIF-8 particles within the liquid cell. (c) TEM image of an area after the cell dried. (d) ED of particles grown in the cell during post-mortem analysis. Reproduced with permission from ref 48. Copyright 2015 American Chemical Society.

doses were around 20× below that measured damage threshold, minimal beam effect on particle assembly or growth occurred, as the kinetics and structural data matched those seen under bulk solution conditions. The formation of smaller subunits in solution demonstrated the formation of ZIF-8 particles. Growth kinetics of individual particles showed a reaction-limited process, and variation of metal:ligand ratio caused increased growth rate, with the formation of larger particles. However, LCTEM provides a unique window into such processes only if certain conditions are met, such as verifying the structure after the LCTEM experiment. Thus, beyond the adequate dose range of the investigated ZIF-8 particles, electron diffraction of the particles following the LCTEM experiment confirmed the observed ZIF-8 structure. This type of post-mortem structure verification is not possible for amorphous materials, which presents new challenges to the field and for mechanisms where phase transitions from amorphous seeds in early growth stages confound exact structure determination. A combination of LCTEM with cryo-TEM, which provides HRTEM of early time synthetic solutions,[79] and small-angle X-ray scattering (SAXS), which enables bulk measurements identifying heterogeneity,[80] may provide more comprehensive and detailed mechanistic information on MOF seeding and growth.

Similarly, LCTEM studies revealed the growth mechanisms of 1D MOFs, known as metal−organic nanotubes (MONTs) with a formula of $[(L1)Cu_2Br_2]$ (L1 = 1,4-bis((4H-1,2,4-triazol-4-yl)methyl)naphthalene).[49] These processes were observed by mixing ligands and metals with temperature variation (VT-LCTEM),[81] providing a glimpse into the future of these methods that allows true chemical reactivity to be studied and varied. The onset of beam damage was from 10 $e^{-}Å^{-2}$ when acquired with an electron dose rate of 0.05 $e^{-}Å^{-2}s^{-1}$. Prolonged irradiation led to dissolution of MONT particles and formation of secondary aggregates. Large fibril-

https://dx.doi.org/10.1021/jacs.0c08773
J. Am. Chem. Soc. 2020, 142, 17224−17235

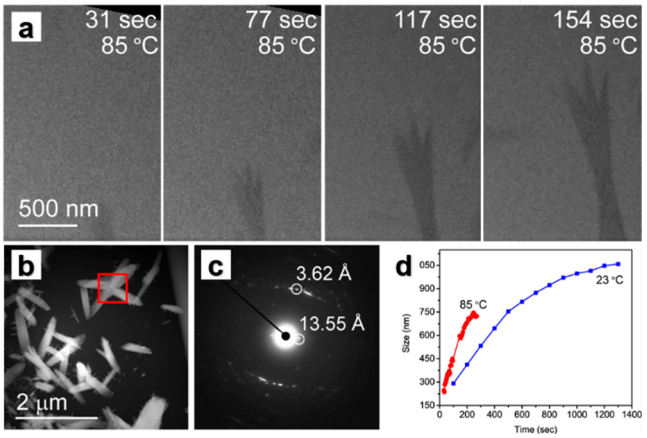

Figure 12. (a) LCTEM snapshots of formation of MONTs with a formula of $[(L1)Cu_2Br_2]$. (b) Fully grown MONT during post-mortem analysis. (c) ED of MONT grown in the cell. (d) Size of MONT plotted as a function of time. Reproduced with permission from ref 49. Copyright 2019 American Chemical Society.

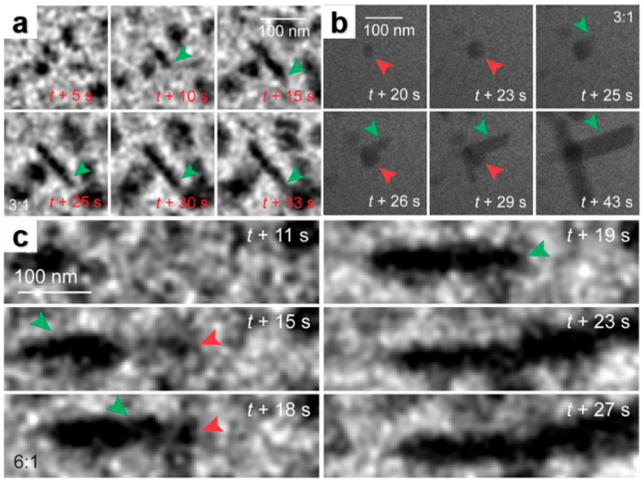

Figure 13. LCTEM snapshots of MONT bundles growing via different mechanisms. Red arrows point to the primary particles, and green arrows point to the nanotubes. Reproduced with permission from ref 50. Copyright 2020 American Chemical Society.

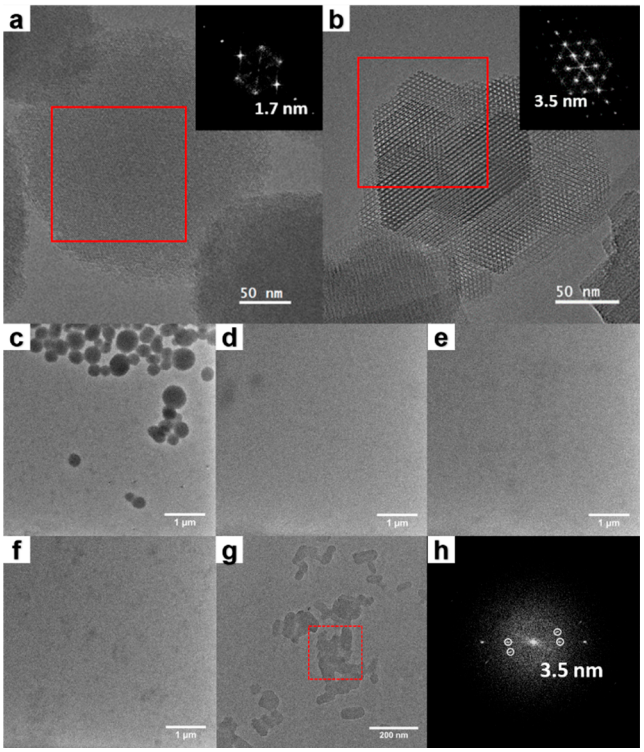

Figure 14. HRTEM of (a) NU-906 and (b) NU-1008, with insets of FFT patterns of the red square areas. LCTEM images with DMF/formic acid = 3:1 at 80 °C, showing the formation of NU-1008 particles: (c) dry cell and (d) wet cell right before heating to 80 °C with NU-906 particles inside, (e) after 10 min and (f) after 20 min at 80 °C; (g) NU-1008 particles grown in the cell during post-mortem analysis; (h) FFT of the area inside the red square of part g. Reproduced with permission from ref 41. Copyright 2020 American Chemical Society.

like MONT bundles formed within the liquid cell (Figure 12a–c). Growth evolution over time (Figure 12d) showed a continuous transformation of monomer to crystalline anisotropic structure driven by a thermodynamic process where the precursor ions seek the lowest energy face of the growing crystal that leads to anisotropic MONT crystals. This process was almost three times faster at 85 °C than at room temperature.

Further LCTEM studies on the seed and growth of similar MONTs formed by ditriazole ligand and silver nitrate with a formula of $[(L2)Ag_2(NO_3)_2(NMP)]$ (L2 = 4,4′-(1,4-(xylene)-diyl)bis(1,2,4-triazole), NMP = *N*-methyl-2-pyrrolidone) revealed that not all MONT nanocrystals grow by classical monomer attachment mechanism, instead variation in the metal:ligand ratio deviates from the classical pathway to allow for multiple indirect pathways that simultaneously exist within the same reaction.[50] Depending on the local availability and depletion of reactants, precursor ions, and amorphous clusters, MONT crystals grow by the continuous transformation of the supersaturated solution into crystalline MONTs (Figure 13a), by heterogeneous nucleation of MONT crystals on the surface of primary particles (Figure 13b), and by coalescence of primary particles that are not commonly observed in MOF chemistry (Figure 13c).

2.2.2. Phase Transitions. In addition to MOF particle formation, LCTEM has been employed in the development of mechanistic insights into polymorph transformations. LCTEM monitored a phase transition driven by formic acid from a microporous MOF, NU-906 ($[Zr_6O_4(OH)_4(TCPB\text{-}Br_2)_2(OH)_4(H_2O)_4]$, TCPB-$Br_2$ = 1,4-dibromo-2,3,5,6-tetrakis(4-carboxyphenyl)benzene; **scu** net; Figure 14a), to a mesoporous MOF, NU-1008 ($[Zr_6O_4(OH)_4(TCPB\text{-}Br_2)_2(OH)_3(HCOO)(H_2O)_3]$; **csq** net; Figure 14b) indicated that the phase transition followed a dissolution-reprecipitation pathway.[41] The dissolution of NU-906 occurred with a low concentration of formic acid (DMF/formic acid = 7:1). Separately, a higher concentration of formic acid (DMF/formic acid = 3:1) promoted the reprecipitation of NU-1008 (Figure 14c–h). Interestingly, an intermediate concentration of formic acid (DMF/formic acid = 5:1) resulted in the two processes occurring concurrently. Formic acid facilitated the dissolution of NU-906, which resulted in an intermediate solution with the same building units as the starting synthetic solution of NU-1008. Therefore, the dissolution of NU-906 concurrently generated NU-1008. These LCTEM results were consistent with the in situ PXRD measurements which showed a decreased amount of NU-906 with the formation of NU-1008. The combination of the two techniques here provides an

https://dx.doi.org/10.1021/jacs.0c08773
J. Am. Chem. Soc. 2020, 142, 17224–17235

example that different types of in situ techniques—examining individual particles or bulk—could correlate with each other to investigate dynamic processes of crystalline materials.

2.2.3. Carbonization. While in situ LCTEM specializes in the examination of dynamics in liquid phase, in situ hot stage TEM allows for the observation of dynamics in solid state. The carbonization of MOFs could generate MOF derivations, where MOFs serve as precursors and templates to synthesize functional materials for energy and environmental applications.[82] The carbonization of a Ni-MOF ($[Ni_2(PTCA)(H_2O)_2]$, PTCA = 3,4,9,10-perylenetetracarboxylate) was investigated through in situ hot stage experiments from room temperature to 700 °C.[47] When the samples were heated up to 700 °C, TEM images and ED patterns indicated changes in the Ni-MOF. With an increase in temperature, the Ni-MOF was gradually degraded and Ni nanoparticles were formed in the carbon matrix at 400 °C. The crystallinity of the Ni nanoparticles and the stability of carbon matrix were gradually enhanced with elevated temperature. Some Ni nanoparticles escaped from the matrix and were aggregated into large faceted Ni particles once the temperature reached 700 °C. In situ hot stage TEM studies elucidate thermal stabilities and mechanisms of thermal decomposition of MOFs,[39] which could indicate temperature-dependent behaviors of individual MOF particles during the processes of TGA measurement.

2.2.4. Flexible "Breathing" MOFs. Flexible MOFs can undergo reversible structural transitions, or pore "breathing", through guest molecule adsorption and desorption processes, accompanied by changes of unit cell parameters. Investigation to the underlying process of this phenomenon at the molecular level can provide fundamental insights into host–guest interactions. In situ ETEM was used to directly monitor the breathing processes of MIL-53(Cr) ([Cr(OH)(bdc)], **sra** net) nanocrystals during water molecule adsorption and desorption.[36] The ETEM gas manifold system introduced water vapor to the specimen, while a hot stage holder controlled the temperature. First, the crystal pores were evacuated of residual linker and solvent molecules upon treatment with ultrahigh vacuum and beam irradiation. A dramatic transition happened under water vapor upon heating the sample to 300 °C, and 1 water molecule was adsorbed per unit cell as determined by ED with molecular dynamics simulations. After the system returned to room temperature, future lattice change confirmed the adsorption of 24 additional water molecules. Thus, the initially adsorbed water molecules formed hydrogen bonds with the bridging μ–OH groups of MIL-53(Cr), which activated the breathing effect by providing more effective hydrogen bonding sites for additional water molecules. This ETEM study opens the door to in situ investigations toward adsorption and desorption processes of flexible MOFs. Future work can create various environments by introducing different types of gases to the specimen,[83,84] and the observed molecular level behavior could correlate with the MOF isotherms, driving us to engineer pore "breathing".

2.2.5. Postsynthetic Exchange. Postsynthetic exchange (PSE) of metal nodes or linkers is an important type of processing method applied to MOFs to expand their functionalities. Careful and thorough characterization remains critical to monitor the dynamic changes and to confirm the final structures. TEM techniques can determine the structure and composition of individual MOF particles after these manipulations. Even though the employed techniques here are not in situ, they offer unparalleled information to the complete analysis of these important dynamic changes. STEM with EDS and EELS studied the metal-based PSE processes of UiO-66(Zr) with Ti^{4+} and Hf^{4+}.[85] Surprisingly, these TEM techniques revealed deposition of metal oxide coatings on UiO-66(Zr), rather than the expected metal-based exchange processes.[86−89] Under TEM, the MOF particles displayed features of exterior nanoscale coating on particles after PSE, which was not observable by SEM. STEM-EDS and STEM-EELS characterizations showed single crystalline Zr-MOF cores with HfO_2 shells (Figure 15). The same techniques

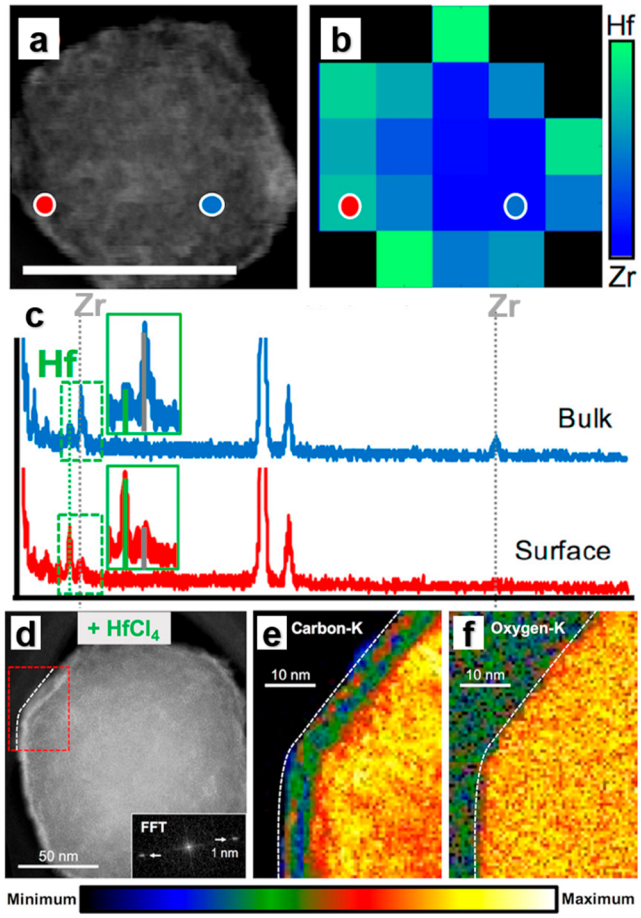

Figure 15. STEM-EDS of UiO-66(Zr) + $HfCl_4$: (a) STEM image, (b) Hf:Zr atomic ratio map, and (c) EDS spectra from the surface (red) and interior (blue) regions. STEM-EELS of UiO-66(Zr) + $HfCl_4$: (d) STEM image and EELS spectral maps of (e) Carbon-K and (f) Oxygen-K for the region marked by the red box. Reproduced with permission from ref 85. Copyright 2017 American Chemical Society.

confirmed the successful ligand-based PSE processes of UiO-66(Zr) with bromo- and iodo-functionalized bdc^{2-} linkers with a resulting uniform distribution of Br and I throughout the particles. Clearly, elemental mapping by TEM techniques can prove indispensable to elucidate structural changes for these postsynthetic manipulations, especially in cases of possible deposition or displacement of metals.

3. CONCLUSIONS AND PERSPECTIVES

The development and implementation of TEM methodologies has transformed our fundamental understanding of MOF structure and, most recently, dynamics. TEM techniques

https://dx.doi.org/10.1021/jacs.0c08773
J. Am. Chem. Soc. 2020, 142, 17224−17235

resolve nanocrystal structures that cannot be determined by X-ray diffraction methods. Moreover, TEM allows for the study of the surface and interfacial structures of MOFs, defects, and host−guest interactions. The nascent collection of in situ TEM techniques provides direct spatiotemporal observation on MOF dynamics, promoting a new phase of mechanistic understanding of MOF formation, particle growth, phase transitions, and pore breathing.

We envision that TEM will continue to provide critical insights and will become an expected and essential characterization technique for MOFs. The method is complementary to other conventional characterization techniques that remain the cornerstones of the field. The development and wider applications of 3D-ED and HRTEM with low dose conditions have the potential to realize structure determination of most nano- and micron-sized MOFs, which reduces the necessity of laborious screening of reaction conditions for large single crystal MOFs.

Cryo-TEM offers opportunities for the observation of a wide range of guest molecules in MOFs, providing detailed information about host−guest interactions. Molecular-scale insights into locations and local behaviors of guest molecules inside the pores of MOFs will elucidate fundamental structural information, further guiding the design and synthesis of host−guest MOF systems as functional composite materials with diverse potential applications.

More advanced TEM techniques, driven by the development of detector technologies and computational and image analysis methods, will be applied to MOF characterization. The application of 4-dimensional scanning transmission electron microscopy (4D-STEM)[90,91] can realize phase, orientation, and grain boundary mapping of MOF films in high resolution and over large areas. The use of ultrahigh readout speed DDEC camera will achieve recording of ∼ms to ∼μs processes involving molecular assemblies, nucleation and growth mechanisms, and other dynamic processes, taking these in situ investigations to the next level. High resolution spectroscopic imaging at subunit-cell scale remains elusive within MOFs due to their beam sensitivities. However, the low-dose and cryogenic conditions that lessen beam damage as well as the development of detectors hold the potential to elucidate elemental distributions of mix-metal MOFs, interlayer structures of 2D-MOFs, and other complicated multicomponent systems.

Finally, a lack of fundamental insights into the mechanism of beam damage on MOFs and the effect of various structural parameters on the resulting beam sensitivities complicates the study of MOF materials with TEM today. A systematic study of MOF beam sensitivities over their metal nodes, linkers, topologies, guest molecules, and other factors will allow researchers to achieve a more fundamental and comprehensive understanding of the correlation between MOF structural parameters and their structures elucidated by TEM. Insights into the solution and gas phase performance of these materials via advanced TEM methods enabling this type of imaging have begun opening up new opportunities for synthetic chemists. Ultimately, our ability to observe phenomena and determine structures makes possible new diversity of chemical reactivity and function. Given the exciting trajectory of the field, the coming years will see HRTEM methods increasingly paired with solution phase and gas phase studies for next generation materials.

AUTHOR INFORMATION

Corresponding Authors

Seth M. Cohen − *Department of Chemistry and Biochemistry, University of California, San Diego, La Jolla, California 92093-0358, United States;* orcid.org/0000-0002-5233-2280; Email: scohen@ucsd.edu

Omar K. Farha − *Department of Chemistry and International Institute of Nanotechnology, Northwestern University, Evanston, Illinois 60208, United States;* orcid.org/0000-0002-9904-9845; Email: o-farha@northwestern.edu

Nathan C. Gianneschi − *Department of Chemistry and International Institute of Nanotechnology and Department of Biomedical Engineering, Materials Science & Engineering, Pharmacology, Simpson-Querrey Institute, Chemistry of Life Processes Institute, Lurie Cancer Center, Northwestern University, Evanston, Illinois 60208, United States; Department of Chemistry and Biochemistry, University of California, San Diego, La Jolla, California 92093-0358, United States;* orcid.org/0000-0001-9945-5475; Email: nathan.gianneschi@northwestern.edu

Authors

Xinyi Gong − *Department of Chemistry and International Institute of Nanotechnology, Northwestern University, Evanston, Illinois 60208, United States;* orcid.org/0000-0003-0295-3959

Karthikeyan Gnanasekaran − *Department of Chemistry and International Institute of Nanotechnology, Northwestern University, Evanston, Illinois 60208, United States;* orcid.org/0000-0001-6635-0888

Zhijie Chen − *Department of Chemistry and International Institute of Nanotechnology, Northwestern University, Evanston, Illinois 60208, United States;* orcid.org/0000-0001-9232-7382

Lee Robison − *Department of Chemistry and International Institute of Nanotechnology, Northwestern University, Evanston, Illinois 60208, United States;* orcid.org/0000-0002-7419-4499

Megan C. Wasson − *Department of Chemistry and International Institute of Nanotechnology, Northwestern University, Evanston, Illinois 60208, United States;* orcid.org/0000-0002-9384-2033

Kyle C. Bentz − *Department of Chemistry and Biochemistry, University of California, San Diego, La Jolla, California 92093-0358, United States*

Complete contact information is available at: https://pubs.acs.org/10.1021/jacs.0c08773

Notes

The authors declare no competing financial interest.

ACKNOWLEDGMENTS

O.K.F. and N.C.G. gratefully acknowledge support from National Science Foundation's MRSEC program (grant number NSF DMR-1720139). In situ TEM studies of MOF materials were supported by a grant from Army Research Office (grant number W911NF-181-0359). O.K.F. is grateful for the financial support from the Army Research Office (Grant W911NF-191-0340) and the Air Force Research Laboratory (FA8650-15-2-5518). X.G. is supported by the Ryan Fellowship and the Northwestern University International Institute for Nanotechnology. M.C.W. is supported by

the NSF Graduate Research Fellowship under grant DGE-1842165. K.G. acknowledges a postdoctoral fellowship from the Human Frontier Science Program (LT000869/2018-C). K.C.B. acknowledges support from the Research Corporation for Science Advancement (RCSA) through the Cottrell Fellowship Initiative, which is partially funded by a National Science Foundation award to the RCSA (CHE-2039044). The synthesis of polyMOFs was supported by a grant from the Department of Energy, Office of Basic Energy Sciences, Division of Materials Science and Engineering under Award No. DE-FG02-08ER46519.

REFERENCES

(1) Furukawa, H.; Cordova, K. E.; O'Keeffe, M.; Yaghi, O. M. The Chemistry and Applications of Metal-Organic Frameworks. *Science* **2013**, *341* (6149), 974.
(2) Kitagawa, S. Future Porous Materials. *Acc. Chem. Res.* **2017**, *50* (3), 514−516.
(3) Yuan, S.; Feng, L.; Wang, K. C.; Pang, J. D.; Bosch, M.; Lollar, C.; Sun, Y. J.; Qin, J. S.; Yang, X. Y.; Zhang, P.; Wang, Q.; Zou, L. F.; Zhang, Y. M.; Zhang, L. L.; Fang, Y.; Li, J. L.; Zhou, H. C. Stable Metal-Organic Frameworks: Design, Synthesis, and Applications. *Adv. Mater.* **2018**, *30* (37), 1704303.
(4) Chen, Z.; Jiang, H.; Li, M.; O'Keeffe, M.; Eddaoudi, M. Reticular Chemistry 3.2: Typical Minimal Edge-Transitive Derived and Related Nets for the Design and Synthesis of Metal-Organic Frameworks. *Chem. Rev.* **2020**, *120* (16), 8039−8065.
(5) Jiang, J. C.; Furukawa, H.; Zhang, Y. B.; Yaghi, O. M. High Methane Storage Working Capacity in Metal-Organic Frameworks with Acrylate Links. *J. Am. Chem. Soc.* **2016**, *138* (32), 10244−10251.
(6) Chen, Z. J.; Li, P. H.; Anderson, R.; Wang, X. J.; Zhang, X.; Robison, L.; Redfern, L. R.; Moribe, S.; Islamoglu, T.; Gomez-Gualdron, D. A.; Yildirim, T.; Stoddart, J. F.; Farha, O. K. Balancing volumetric and gravimetric uptake in highly porous materials for clean energy. *Science* **2020**, *368* (6488), 297.
(7) Li, B.; Wen, H. M.; Zhou, W.; Xu, J. Q.; Chen, B. L. Porous Metal-Organic Frameworks: Promising Materials for Methane Storage. *Chem.* **2016**, *1* (4), 557−580.
(8) Kapelewski, M. T.; Runcevski, T.; Tarver, J. D.; Jiang, H. Z. H.; Hurst, K. E.; Parilla, P. A.; Ayala, A.; Gennett, T.; FitzGerald, S. A.; Brown, C. M.; Long, J. R. Record High Hydrogen Storage Capacity in the Metal-Organic Framework Ni-2(m-dobdc) at Near-Ambient Temperatures. *Chem. Mater.* **2018**, *30* (22), 8179−8189.
(9) Li, H.; Wang, K. C.; Sun, Y. J.; Lollar, C. T.; Li, J. L.; Zhou, H. C. Recent advances in gas storage and separation using metal-organic frameworks. *Mater. Today* **2018**, *21* (2), 108−121.
(10) Cui, X. L.; Chen, K. J.; Xing, H. B.; Yang, Q. W.; Krishna, R.; Bao, Z. B.; Wu, H.; Zhou, W.; Dong, X. L.; Han, Y.; Li, B.; Ren, Q. L.; Zaworotko, M. J.; Chen, B. L. Pore chemistry and size control in hybrid porous materials for acetylene capture from ethylene. *Science* **2016**, *353* (6295), 141−144.
(11) Cadiau, A.; Adil, K.; Bhatt, P. M.; Belmabkhout, Y.; Eddaoudi, M. A metal-organic framework-based splitter for separating propylene from propane. *Science* **2016**, *353* (6295), 137−140.
(12) Banerjee, D.; Cairns, A. J.; Liu, J.; Motkuri, R. K.; Nune, S. K.; Fernandez, C. A.; Krishna, R.; Strachan, D. M.; Thallapally, P. K. Potential of Metal-Organic Frameworks for Separation of Xenon and Krypton. *Acc. Chem. Res.* **2015**, *48* (2), 211−219.
(13) Zhang, T.; Lin, W. B. Metal-organic frameworks for artificial photosynthesis and photocatalysis. *Chem. Soc. Rev.* **2014**, *43* (16), 5982−5993.
(14) Yoon, M.; Srirambalaji, R.; Kim, K. Homochiral Metal-Organic Frameworks for Asymmetric Heterogeneous Catalysis. *Chem. Rev.* **2012**, *112* (2), 1196−1231.
(15) Liu, J. W.; Chen, L. F.; Cui, H.; Zhang, J. Y.; Zhang, L.; Su, C. Y. Applications of metal-organic frameworks in heterogeneous supramolecular catalysis. *Chem. Soc. Rev.* **2014**, *43* (16), 6011−6061.
(16) Wasson, M. C.; Buru, C. T.; Chen, Z. J.; Islamoglu, T.; Farha, O. K. Metal-organic frameworks: A tunable platform to access single-site heterogeneous catalysts. *Appl. Catal., A* **2019**, *586*, 117214.
(17) Hanikel, N.; Prevot, M. S.; Yaghi, O. M. MOF water harvesters. *Nat. Nanotechnol.* **2020**, *15*, 348−355.
(18) Rieth, A. J.; Wright, A. M.; Dinca, M. Kinetic stability of metal-organic frameworks for corrosive and coordinating gas capture. *Nat. Rev. Mater.* **2019**, *4* (11), 708−725.
(19) Abtab, S. M. T.; Alezi, D.; Bhatt, P. M.; Shkurenko, A.; Belmabkhout, Y.; Aggarwal, H.; Weselinski, L. J.; Alsadun, N.; Samin, U.; Hedhili, M. N.; Eddaoudi, M. Reticular Chemistry in Action: A Hydrolytically Stable MOF Capturing Twice Its Weight in Adsorbed Water. *Chem.* **2018**, *4* (1), 94−105.
(20) Chen, Z. J.; Li, P. H.; Zhang, X.; Li, P.; Wasson, M. C.; Islamoglu, T.; Stoddart, J. F.; Farha, O. K. Reticular Access to Highly Porous acs-MOFs with Rigid Trigonal Prismatic Linkers for Water Sorption. *J. Am. Chem. Soc.* **2019**, *141* (7), 2900−2905.
(21) Horcajada, P.; Chalati, T.; Serre, C.; Gillet, B.; Sebrie, C.; Baati, T.; Eubank, J. F.; Heurtaux, D.; Clayette, P.; Kreuz, C.; Chang, J.-S.; Hwang, Y. K.; Marsaud, V.; Bories, P.-N.; Cynober, L.; Gil, S.; Férey, G.; Couvreur, P.; Gref, R. Porous metal−organic-framework nanoscale carriers as a potential platform for drug delivery and imaging. *Nat. Mater.* **2010**, *9*, 172−178.
(22) Simon-Yarza, T.; Mielcarek, A.; Couvreur, P.; Serre, C. Nanoparticles of Metal-Organic Frameworks: On the Road to In Vivo Efficacy in Biomedicine. *Adv. Mater.* **2018**, *30* (37), 1707365.
(23) Chen, Y.; Li, P.; Modica, J. A.; Drout, R. J.; Farha, O. K. Acid-Resistant Mesoporous Metal-Organic Framework toward Oral Insulin Delivery: Protein Encapsulation, Protection, and Release. *J. Am. Chem. Soc.* **2018**, *140* (17), 5678−5681.
(24) Cohen, S. M. The Postsynthetic Renaissance in Porous Solids. *J. Am. Chem. Soc.* **2017**, *139* (8), 2855−2863.
(25) Islamoglu, T.; Goswami, S.; Li, Z. Y.; Howarth, A. J.; Farha, O. K.; Hupp, J. T. Postsynthetic Tuning of Metal-Organic Frameworks for Targeted Applications. *Acc. Chem. Res.* **2017**, *50* (4), 805−813.
(26) Egerton, R. F. Mechanisms of radiation damage in beam-sensitive specimens, for TEM accelerating voltages between 10 and 300 kV. *Microsc. Res. Tech.* **2012**, *75* (11), 1550−1556.
(27) Ugurlu, O.; Haus, J.; Gunawan, A. A.; Thomas, M. G.; Maheshwari, S.; Tsapatsis, M.; Mkhoyan, K. A. Radiolysis to knock-on damage transition in zeolites under electron beam irradiation. *Phys. Rev. B: Condens. Matter Mater. Phys.* **2011**, *83* (11), 113408.
(28) Kotakoski, J.; Santos-Cottin, D.; Krasheninnikov, A. V. Stability of Graphene Edges under Electron Beam: Equilibrium Energetics versus Dynamic Effects. *ACS Nano* **2012**, *6* (1), 671−676.
(29) Wiktor, C.; Turner, S.; Zacher, D.; Fischer, R. A.; Tendeloo, G. V. Imaging of intact MOF-5 nanocrystals by advanced TEM at liquid nitrogen temperature. *Microporous Mesoporous Mater.* **2012**, *162*, 131−135.
(30) Henderson, R. Cryoprotection of Protein Crystals against Radiation-Damage in Electron and X-Ray-Diffraction. *Proc. R. Soc. London, Ser. B* **1990**, *241* (1300), 6−8.
(31) Egerton, R. F.; Li, P.; Malac, M. Radiation damage in the TEM and SEM. *Micron* **2004**, *35* (6), 399−409.
(32) Taylor, K. A.; Glaeser, R. M. Retrospective on the early development of cryoelectron microscopy of macromolecules and a prospective on opportunities for the future. *J. Struct. Biol.* **2008**, *163* (3), 214−223.
(33) Kourkoutis, L. F.; Plitzko, J. M.; Baumeister, W. Electron Microscopy of Biological Materials at the Nanometer Scale. *Annu. Rev. Mater. Res.* **2012**, *42*, 33−58.
(34) Xiao, B.; Byrne, P. J.; Wheatley, P. S.; Wragg, D. S.; Zhao, X.; Fletcher, A. J.; Thomas, K. M.; Peters, L.; Evans, J. S.; Warren, J. E.; Zhou, W.; Morris, R. E. Chemically blockable transformation and ultraselective low-pressure gas adsorption in a non-porous metal organic framework. *Nat. Chem.* **2009**, *1* (4), 289−294.
(35) Li, X.; Wang, J.; Liu, X.; Liu, L.; Cha, D.; Zheng, X.; Yousef, A. A.; Song, K.; Zhu, Y.; Zhang, D.; Han, Y. Direct Imaging of Tunable Crystal Surface Structures of MOF MIL-101 Using High-Resolution

https://dx.doi.org/10.1021/jacs.0c08773
J. Am. Chem. Soc. 2020, 142, 17224−17235

Electron Microscopy. *J. Am. Chem. Soc.* **2019**, *141* (30), 12021−12028.
(36) Parent, L. R.; Pham, C. H.; Patterson, J. P.; Denny, M. S.; Cohen, S. M.; Gianneschi, N. C.; Paesani, F. Pore Breathing of Metal-Organic Frameworks by Environmental Transmission Electron Microscopy. *J. Am. Chem. Soc.* **2017**, *139* (40), 13973−13976.
(37) Deng, H. X.; Grunder, S.; Cordova, K. E.; Valente, C.; Furukawa, H.; Hmadeh, M.; Gandara, F.; Whalley, A. C.; Liu, Z.; Asahina, S.; Kazumori, H.; O'Keeffe, M.; Terasaki, O.; Stoddart, J. F.; Yaghi, O. M. Large-Pore Apertures in a Series of Metal-Organic Frameworks. *Science* **2012**, *336* (6084), 1018−1023.
(38) Zhu, Y.; Ciston, J.; Zheng, B.; Miao, X.; Czarnik, C.; Pan, Y.; Sougrat, R.; Lai, Z.; Hsiung, C. E.; Yao, K.; Pinnau, I.; Pan, M.; Han, Y. Unravelling surface and interfacial structures of a metal-organic framework by transmission electron microscopy. *Nat. Mater.* **2017**, *16* (5), 532−536.
(39) Zhang, D. L.; Zhu, Y. H.; Liu, L. M.; Ying, X. R.; Hsiung, C. E.; Sougrat, R.; Li, K.; Han, Y. Atomic-resolution transmission electron microscopy of electron beam-sensitive crystalline materials. *Science* **2018**, *359* (6376), 675.
(40) Gong, X.; Noh, H.; Gianneschi, N. C.; Farha, O. K. Interrogating Kinetic versus Thermodynamic Topologies of Metal-Organic Frameworks via Combined Transmission Electron Microscopy and X-ray Diffraction Analysis. *J. Am. Chem. Soc.* **2019**, *141* (15), 6146−6151.
(41) Lyu, J.; Gong, X.; Lee, S. J.; Gnanasekaran, K.; Zhang, X.; Wasson, M. C.; Wang, X.; Bai, P.; Guo, X.; Gianneschi, N. C.; Farha, O. K. Phase Transitions in Metal-Organic Frameworks Directly Monitored through In Situ Variable Temperature Liquid-Cell Transmission Electron Microscopy and In Situ X-ray Diffraction. *J. Am. Chem. Soc.* **2020**, *142* (10), 4609−4615.
(42) Jin, L.; Milazzo, A. C.; Kleinfelder, S.; Li, S.; Leblanc, P.; Duttweiler, F.; Bouwer, J. C.; Peltier, S. T.; Ellisman, M. H.; Xuong, N. H. Applications of direct detection device in transmission electron microscopy. *J. Struct. Biol.* **2008**, *161* (3), 352−358.
(43) Li, X.; Mooney, P.; Zheng, S.; Booth, C. R.; Braunfeld, M. B.; Gubbens, S.; Agard, D. A.; Cheng, Y. Electron counting and beam-induced motion correction enable near-atomic-resolution single-particle cryo-EM. *Nat. Methods* **2013**, *10* (6), 584−90.
(44) Klinger, M.; Jager, A. Crystallographic Tool Box (CrysTBox): automated tools for transmission electron microscopists and crystallographers. *J. Appl. Crystallogr.* **2015**, *48*, 2012−2018.
(45) Zhang, Y.; Yan, R.; Sun, T.; Ma, Y. A simple program for fast tilting electron-beam sensitive crystals to zone axes. *Ultramicroscopy* **2020**, *211*, 112941.
(46) Liu, L.; Chen, Z.; Wang, J.; Zhang, D.; Zhu, Y.; Ling, S.; Huang, K. W.; Belmabkhout, Y.; Adil, K.; Zhang, Y.; Slater, B.; Eddaoudi, M.; Han, Y. Imaging defects and their evolution in a metal-organic framework at sub-unit-cell resolution. *Nat. Chem.* **2019**, *11* (7), 622−628.
(47) Xu, D.; Zhang, D.; Zou, H.; Zhu, L.; Xue, M.; Fang, Q.; Qiu, S. Guidance from an in situ hot stage in TEM to synthesize magnetic metal nanoparticles from a MOF. *Chem. Commun.* **2016**, *52* (69), 10513−10516.
(48) Patterson, J. P.; Abellan, P.; Denny, M. S.; Park, C.; Browning, N. D.; Cohen, S. M.; Evans, J. E.; Gianneschi, N. C. Observing the Growth of Metal-Organic Frameworks by in Situ Liquid Cell Transmission Electron Microscopy. *J. Am. Chem. Soc.* **2015**, *137* (23), 7322−7328.
(49) Vailonis, K. M.; Gnanasekaran, K.; Powers, X. B.; Gianneschi, N. C.; Jenkins, D. M. Elucidating the Growth of Metal-Organic Nanotubes Combining Isoreticular Synthesis with Liquid-Cell Transmission Electron Microscopy. *J. Am. Chem. Soc.* **2019**, *141* (26), 10177−10182.
(50) Gnanasekaran, K.; Vailonis, K. M.; Jenkins, D. M.; Gianneschi, N. C. In Situ Monitoring of the Seeding and Growth of Silver Metal−Organic Nanotubes by Liquid-Cell Transmission Electron Microscopy. *ACS Nano* **2020**, *14* (7), 8735−8743.
(51) Denysenko, D.; Grzywa, M.; Tonigold, M.; Streppel, B.; Krkljus, I.; Hirscher, M.; Mugnaioli, E.; Kolb, U.; Hanss, J.; Volkmer, D. Elucidating gating effects for hydrogen sorption in MFU-4-type triazolate-based metal-organic frameworks featuring different pore sizes. *Chem. - Eur. J.* **2011**, *17* (6), 1837−1848.
(52) Feyand, M.; Mugnaioli, E.; Vermoortele, F.; Bueken, B.; Dieterich, J. M.; Reimer, T.; Kolb, U.; de Vos, D.; Stock, N. Automated diffraction tomography for the structure elucidation of twinned, sub-micrometer crystals of a highly porous, catalytically active bismuth metal-organic framework. *Angew. Chem., Int. Ed.* **2012**, *51* (41), 10373−10376.
(53) Zhu, L.; Zhang, D.; Xue, M.; Li, H.; Qiu, S. Direct observations of the MOF (UiO-66) structure by transmission electron microscopy. *CrystEngComm* **2013**, *15* (45), 9356.
(54) Wang, B.; Rhauderwiek, T.; Inge, A. K.; Xu, H. Y.; Yang, T. M.; Huang, Z. H.; Stock, N.; Zou, X. D. A Porous Cobalt Tetraphosphonate Metal-Organic Framework: Accurate Structure and Guest Molecule Location Determined by Continuous-Rotation Electron Diffraction. *Chem. - Eur. J.* **2018**, *24* (66), 17429−17433.
(55) Yuan, S.; Qin, J. S.; Xu, H. Q.; Su, J.; Rossi, D.; Chen, Y. P.; Zhang, L. L.; Lollar, C.; Wang, Q.; Jiang, H. L.; Son, D. H.; Xu, H. Y.; Huang, Z. H.; Zou, X. D.; Zhou, H. C. [Ti8Zr2O12(COO)(16)] Cluster: An Ideal Inorganic Building Unit for Photoactive Metal-Organic Frameworks. *ACS Cent. Sci.* **2018**, *4* (1), 105−111.
(56) Liu, Y. Z.; Ma, Y. H.; Zhao, Y. B.; Sun, X. X.; Gandara, F.; Furukawa, H.; Liu, Z.; Zhu, H. Y.; Zhu, C. H.; Suenaga, K.; Oleynikov, P.; Alshammari, A. S.; Zhang, X.; Terasaki, O.; Yaghi, O. M. Weaving of organic threads into a crystalline covalent organic framework. *Science* **2016**, *351* (6271), 365−369.
(57) Huang, Z.; Ge, M.; Carraro, F.; Doonan, C.; Falcaro, P.; Zou, X. Can 3D Electron Diffraction Provide Accurate Atomic Structures of MetalOrganic Frameworks? *Faraday Discuss.* **2020**, DOI: 10.1039/D0FD00015A.
(58) Lebedev, O. I.; Millange, F.; Serre, C.; Van Tendeloo, G.; Ferey, G. First direct imaging of giant pores of the metal-organic framework MIL-101. *Chem. Mater.* **2005**, *17* (26), 6525−6527.
(59) Díaz-García, M.; Mayoral, Á.; Díaz, I.; Sánchez-Sánchez, M. Nanoscaled M-MOF-74 Materials Prepared at Room Temperature. *Cryst. Growth Des.* **2014**, *14* (5), 2479−2487.
(60) Mayoral, A.; Sanchez-Sanchez, M.; Alfayate, A.; Perez-Pariente, J.; Diaz, I. Atomic Observations of Microporous Materials Highly Unstable under the Electron Beam: The Cases of Ti-Doped AlPO4−5 and Zn-MOF-74. *ChemCatChem* **2015**, *7* (22), 3719−3724.
(61) Zhang, Z. J.; Nguyen, H. T. H.; Miller, S. A.; Cohen, S. M. polyMOFs: A Class of Interconvertible Polymer-Metal-Organic-Framework Hybrid Materials. *Angew. Chem., Int. Ed.* **2015**, *54* (21), 6152−6157.
(62) Bentz, K. C.; Cohen, S. M. Supramolecular Metallopolymers: From Linear Materials to Infinite Networks. *Angew. Chem., Int. Ed.* **2018**, *57* (46), 14992−15001.
(63) Bentz, K. C.; Gnanasekaran, K.; Bailey, J. B.; Ayala, S.; Tezcan, F. A.; Gianneschi, N. C.; Cohen, S. M. Inside polyMOFs: Layered Structures in Polymer-Based Metal-Organic Frameworks. *Chem. Sci.* **2020**, DOI: 10.1039/D0SC03651J.
(64) Moh, P. Y.; Cubillas, P.; Anderson, M. W.; Attfield, M. P. Revelation of the Molecular Assembly of the Nanoporous Metal Organic Framework ZIF-8. *J. Am. Chem. Soc.* **2011**, *133* (34), 13304−13307.
(65) Wagia, R.; Strashnov, I.; Anderson, M. W.; Attfield, M. P. Insight and Control of the Crystal Growth of Zeolitic Imidazolate Framework ZIF-67 by Atomic Force Microscopy and Mass Spectrometry. *Cryst. Growth Des.* **2018**, *18* (2), 695−700.
(66) Makiura, R.; Motoyama, S.; Umemura, Y.; Yamanaka, H.; Sakata, O.; Kitagawa, H. Surface nano-architecture of a metal-organic framework. *Nat. Mater.* **2010**, *9* (7), 565−571.
(67) Scherb, C.; Schodel, A.; Bein, T. Directing the structure of metal-organic frameworks by oriented surface growth on an organic monolayer. *Angew. Chem., Int. Ed.* **2008**, *47* (31), 5777−5779.

(68) Fang, Z. L.; Bueken, B.; De Vos, D. E.; Fischer, R. A. Defect-Engineered Metal-Organic Frameworks. *Angew. Chem., Int. Ed.* **2015**, *54* (25), 7234−7254.
(69) Cliffe, M. J.; Wan, W.; Zou, X.; Chater, P. A.; Kleppe, A. K.; Tucker, M. G.; Wilhelm, H.; Funnell, N. P.; Coudert, F. X.; Goodwin, A. L. Correlated defect nanoregions in a metal-organic framework. *Nat. Commun.* **2014**, *5*, 4176.
(70) Midgley, P. A.; Dunin-Borkowski, R. E. Electron tomography and holography in materials science. *Nat. Mater.* **2009**, *8* (4), 271−280.
(71) Turner, S.; Lebedev, O. I.; Schroder, F.; Esken, D.; Fischer, R. A.; Van Tendeloo, G. Direct imaging of loaded metal-organic framework materials (metal@MOF-5). *Chem. Mater.* **2008**, *20* (17), 5622−5627.
(72) Esken, D.; Turner, S.; Lebedev, O. I.; Van Tendeloo, G.; Fischer, R. A. Au@ZIFs: Stabilization and Encapsulation of Cavity-Size Matching Gold Clusters inside Functionalized Zeolite Imidazolate Frameworks, ZIFs. *Chem. Mater.* **2010**, *22* (23), 6393−6401.
(73) Meledina, M.; Turner, S.; Filippousi, M.; Leus, K.; Lobato, I.; Ramachandran, R. K.; Dendooven, J.; Detavernier, C.; Van Der Voort, P.; Van Tendeloo, G. Direct Imaging of ALD Deposited Pt Nanoclusters inside the Giant Pores of MIL-101. *Part. Part. Syst. Char.* **2016**, *33* (7), 382−387.
(74) Rosler, C.; Aijaz, A.; Turner, S.; Filippousi, M.; Shahabi, A.; Xia, W.; Van Tendeloo, G.; Muhler, M.; Fischer, R. A. Hollow Zn/Co Zeolitic Imidazolate Framework (ZIF) and Yolk-Shell Metal@Zn/Co ZIF Nanostructures. *Chem. - Eur. J.* **2016**, *22* (10), 3304−3311.
(75) Zheng, H. Q.; Zhang, Y. N.; Liu, L. F.; Wan, W.; Guo, P.; Nystrom, A. M.; Zou, X. D. One-pot Synthesis of Metal Organic Frameworks with Encapsulated Target Molecules and Their Applications for Controlled Drug Delivery. *J. Am. Chem. Soc.* **2016**, *138* (3), 962−968.
(76) Wu, X. L.; Yue, H.; Zhang, Y. Y.; Gao, X. Y.; Li, X. Y.; Wang, L. C.; Cao, Y. F.; Hou, M.; An, H. X.; Zhang, L.; Li, S.; Ma, J. Y.; Lin, H.; Fu, Y. A.; Gu, H. K.; Lou, W. Y.; Wei, W.; Zare, R. N.; Ge, J. Packaging and delivering enzymes by amorphous metal-organic frameworks. *Nat. Commun.* **2019**, *10*, 5165.
(77) Aulakh, D.; Liu, L. M.; Varghese, J. R.; Xie, H. M.; Islamoglu, T.; Duell, K.; Kung, C. W.; Hsiung, C. E.; Zhang, Y. X.; Drout, R. J.; Farha, O. K.; Dunbar, K. R.; Han, Y.; Wriedt, M. Direct Imaging of Isolated Single-Molecule Magnets in Metal Organic Frameworks. *J. Am. Chem. Soc.* **2019**, *141* (7), 2997−3005.
(78) Li, Y.; Wang, K.; Zhou, W.; Li, Y.; Vila, R.; Huang, W.; Wang, H.; Chen, G.; Wu, G.-H.; Tsao, Y.; Wang, H.; Sinclair, R.; Chiu, W.; Cui, Y. Cryo-EM Structures of Atomic Surfaces and Host-Guest Chemistry in Metal-Organic Frameworks. *Matter* **2019**, *1* (2), 428−438.
(79) Ogata, A. F.; Rakowski, A. M.; Carpenter, B. P.; Fishman, D. A.; Merham, J. G.; Hurst, P. J.; Patterson, J. P. Direct Observation of Amorphous Precursor Phases in the Nucleation of Protein-Metal-Organic Frameworks. *J. Am. Chem. Soc.* **2020**, *142* (3), 1433−1442.
(80) Bailey, J. B.; Zhang, L.; Chiong, J. A.; Ahn, S.; Tezcan, F. A. Synthetic Modularity of Protein-Metal-Organic Frameworks. *J. Am. Chem. Soc.* **2017**, *139* (24), 8160−8166.
(81) Smith, B. J.; Parent, L. R.; Overholts, A. C.; Beaucage, P. A.; Bisbey, R. P.; Chavez, A. D.; Hwang, N.; Park, C.; Evans, A. M.; Gianneschi, N. C.; Dichtel, W. R. Colloidal Covalent Organic Frameworks. *ACS Cent. Sci.* **2017**, *3* (1), 58−65.
(82) Wu, H. B.; Xia, B. Y.; Yu, L.; Yu, X. Y.; Lou, X. W. Porous molybdenum carbide nano-octahedrons synthesized via confined carburization in metal-organic frameworks for efficient hydrogen production. *Nat. Commun.* **2015**, *6*, 6512.
(83) Salles, F.; Ghoufi, A.; Maurin, G.; Bell, R. G.; Mellot-Draznieks, C.; Ferey, G. Molecular Dynamics Simulations of Breathing MOFs: Structural Transformations of MIL-53(Cr) upon Thermal Activation and CO2 Adsorption. *Angew. Chem., Int. Ed.* **2008**, *47* (44), 8487−8491.
(84) Bourrelly, S.; Llewellyn, P. L.; Serre, C.; Millange, F.; Loiseau, T.; Ferey, G. Different adsorption behaviors of methane and carbon dioxide in the isotypic nanoporous metal terephthalates MIL-53 and MIL-47. *J. Am. Chem. Soc.* **2005**, *127* (39), 13519−13521.
(85) Denny, M. S., Jr.; Parent, L. R.; Patterson, J. P.; Meena, S. K.; Pham, H.; Abellan, P.; Ramasse, Q. M.; Paesani, F.; Gianneschi, N. C.; Cohen, S. M. Transmission Electron Microscopy Reveals Deposition of Metal Oxide Coatings onto Metal-Organic Frameworks. *J. Am. Chem. Soc.* **2018**, *140* (4), 1348−1357.
(86) Kim, M.; Cahill, J. F.; Fei, H. H.; Prather, K. A.; Cohen, S. M. Postsynthetic Ligand and Cation Exchange in Robust Metal-Organic Frameworks. *J. Am. Chem. Soc.* **2012**, *134* (43), 18082−18088.
(87) Santaclara, J. G.; Olivos-Suarez, A. I.; Gonzalez-Nelson, A.; Osadchii, D.; Nasalevich, M. A.; van der Veen, M. A.; Kapteijn, F.; Sheveleva, A. M.; Veber, S. L.; Fedin, M. V.; Murray, A. T.; Hendon, C. H.; Walsh, A.; Gascon, J. Revisiting the Incorporation of Ti(IV) in UiO-type Metal-Organic Frameworks: Metal Exchange versus Grafting and Their Implications on Photocatalysis. *Chem. Mater.* **2017**, *29* (21), 8963−8967.
(88) Smith, S. J. D.; Ladewig, B. P.; Hill, A. J.; Lau, C. H.; Hill, M. R. Post-synthetic Ti Exchanged UiO-66 Metal-Organic Frameworks that Deliver Exceptional Gas Permeability in Mixed Matrix Membranes. *Sci. Rep.* **2015**, *5*, 7823.
(89) Lau, C. H.; Babarao, R.; Hill, M. R. A route to drastic increase of CO2 uptake in Zr metal organic framework UiO-66. *Chem. Commun.* **2013**, *49* (35), 3634−3636.
(90) Zewail, A. H. Four-Dimensional Electron Microscopy. *Science* **2010**, *328* (5975), 187−193.
(91) Ophus, C. Four-Dimensional Scanning Transmission Electron Microscopy (4D-STEM): From Scanning Nanodiffraction to Ptychography and Beyond. *Microsc. Microanal.* **2019**, *25* (3), 563−582.

https://dx.doi.org/10.1021/jacs.0c08773
J. Am. Chem. Soc. 2020, 142, 17224−17235